Journal Name

Review

Beyond Intercalation Based Sodium-ion Batteries: Role of Alloying Anodes, Efficient Sodiation Mechanisms and Recent Progress

Eldho Edison, [a] Sivaramapanicker Sreejith, *[b,c] Chwee Teck Lim*[b,c,d] and Srinivasan Madhavi *[a]

Received 00th January 20xx,
Accepted 00th January 20xx

DOI: 10.1039/x0xx00000x

www.rsc.org/

Sodium-ion batteries (SIBs) have received a renewed interest in the recent years and are projected as an alternative to the existing lithium-ion battery (LIB) system. Research on SIBs is impelled by the low cost and abundant supply of sodium-resources, similar electrochemistry of SIB and LIB and the competing electrochemical performance achieved in the recent years. Significant progress has been made in the development of alloying anodes for SIBs which offer high gravimetric and volumetric energy densities when compared to the conventional intercalation based anodes. Recent progress in the field of advanced operando and ex-situ characterization techniques as well as theoretical computational studies have shed light on the sodiation mechanism of these alloying anodes. Herein, we review the recent developments on alloying anodes for SIBs. Primarily Sn, Sb, and P based alloying anodes are focused upon and the progress on Bi, Ge and Si are also discussed. We focus on the sodiation mechanism of these alloying anodes, recently revealed by means of the advanced experimental and computational tools, to enable the design of efficient strategies for enhanced electrochemical performance. We also discuss the synthetic methodologies and novel approaches adopted for alloying anodes to mitigate the challenges faced during the (de)sodiation cycles. The future outlook and issues to be addressed to realize the practical implementation of alloying anodes are also discussed.

1. Introduction

The ever-rising global energy demands and the growing concerns on climate change and environmental pollution exhorts the need to extensively implement renewable and sustainable energy resources including solar, wind and tidal power plants. However, to realize the large-scale implementation of these intermittent energy resources, it is vital to develop reliable and low-cost electrochemical energy storage (EES) systems. Currently, lithium-ion batteries (LIBs) are widely used for the EES applications because of their high energy density and long calendar life. With the proliferation of LIBs in the electric vehicles sector, it is estimated that the global LIB market would be ~53 billion USD by 2024, with the renewable and grid storage applications alone to surpass ~12 billion USD.[1] This increase in the demand, however, is expected to drastically escalate the cost of LIBs in view of the limited availability and sparse distribution of lithium resources.[2-4] Hence, it is crucial to develop alternative battery technologies to meet the future demands for economical energy storage.

Sodium-ion batteries (SIBs) have received significant attention in the recent past owing to the low-cost and abundance of sodium resources.[5, 6] This is evident from the noteworthy research on SIBs over the past decade (**Fig. 1**). Furthermore, sodium is the second lightest alkali metal and has a redox potential of -2.71 V *vs.* SHE (Standard Hydrogen Electrode)-making sodium the next best choice after lithium. In addition, the similarity in operation of SIBs to LIBs is expected to aid the smooth changeover to SIBs. However, the transition from LIB to NIB is expected to impose an energy penalty of ~15% due to the lower redox potential of sodium compared to lithium.[7] At the same time SIBs are expected to bring forth nearly 30% reduction in costs- a remarkable pointer to achieve large format-low cost energy storage systems.[7] However, to realize this transition, it is vital to develop electrodes with high gravimetric and volumetric capacities in addition to optimizing the electrolytes and binders for SIBs.[5, 8, 9]

The progress and expertise achieved in LIB technology over the past decades could be translated to SIB research to expedite the progress in the field. In fact, suites of oxides, [10-18] sulphides[19-23] and sulphates, [24-26] fluorides, [27-30] phosphates[31-37] and fluorophosphates[38-41] have already been developed as potential cathodes for SIBs. Many of these cathodes display electrochemical performances tantamount to the commercial LIB cathodes. However, the progress on SIB anodes seem to be lagging. While graphite, the anode of choice for LIB is found to be unsuitable for sodium intercalation, [42] hard carbon obtained by the pyrolysis of glucose is found to efficiently intercalate

[a] School of Materials Science and Engineering, Nanyang Technological University, 50 Nanyang Avenue, 639798, Singapore. Email: madhavi@ntu.edu.sg
[b] the Center for Advanced 2D Materials (CA2DM), National University of Singapore, 6 Science Drive 2, 117546, Singapore.
[c] Biomedical Institute for Global Health Research and Technology, National University of Singapore, 117599, Singapore. Email: bigsiv@nus.edu.sg ; sreejith.siva@gmail.com
[d] Department of Biomedical Engineering, National University of Singapore, 2 Engineering Drive 3, 117581, Singapore. Email: ctlim@nus.edu.sg

sodium at a potential close to 0 V *vs.* Na.[43] Nevertheless, the low volumetric and gravimetric energy densities of hard carbon

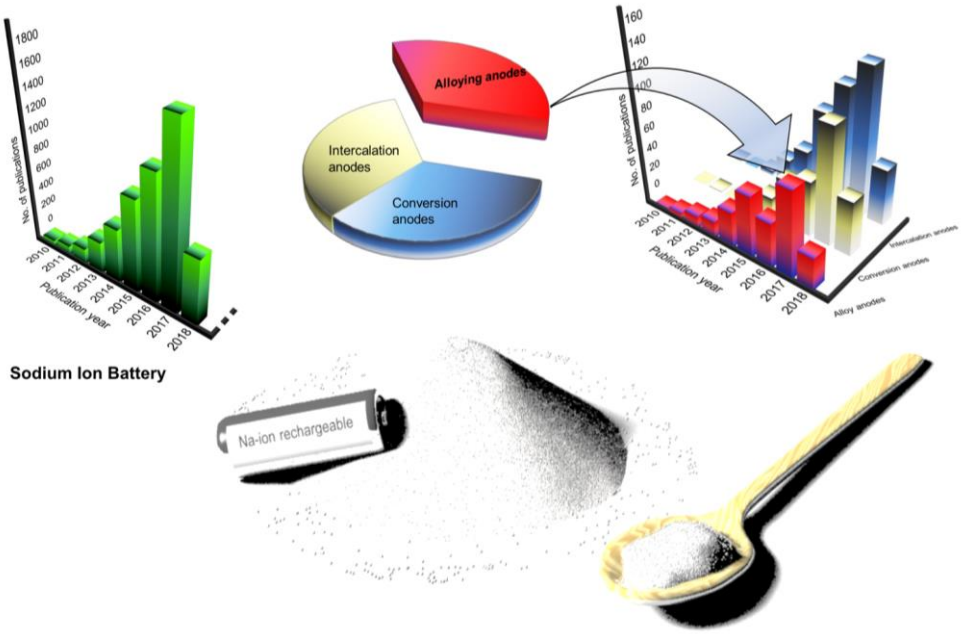

Fig. 1 Large-format, low-cost SIBs for stationary electrochemical energy storage and research progress in SIB and alloy anodes for SIB. (Data source: Web of Science, 01-May-2018).

call forth the development of high capacity anodes for SIBs which is crucial to achieving the target of large-format and inexpensive SIBs.[44-49] In this regard, sodium alloying anodes offering high sodiation capacities are expected to lead the way. Among others, tin, antimony and phosphorous offer high sodiation capacities by forming Na_xM (M=Sn, Sb, P) phases at room temperature. At the same time, these alloy anodes suffer from huge volume changes causing pulverization and cracking of the active materials upon sodiation-leading to fast capacity decay. To overcome these challenges, it is essential to develop an understanding of the sodiation mechanism in these alloying anodes. Furthermore, various strategies have been adopted to confront these challenges, including optimizing the structural design of the active material, use of intermetallics and carbon-based matrices to buffer volume changes and the optimization of electrolyte and binder to stabilize the solid electrolyte interphase (SEI) are a few among others.

It is worth mentioning that several excellent review articles highlighting the progress in SIBs have been reported in the recent past.[5, 6, 8, 9, 50-58] At the same time, we believe that a review on alloying anodes with a focus on the sodiation mechanism would help researchers to gain insight and accelerate the progress in this field. In this review, the sodiation mechanism of the promising alloying anodes for SIB- tin, antimony and phosphorus (**Fig. 2**) is presented from recent literature by both computational and experimental insights. The recent progress and novel strategies employed in each of these alloying anodes are described and the progress of bismuth, germanium and silicon-based anodes for SIBs are also reviewed. A few practical approaches that can improve the electrochemical performance of alloying anodes are discussed. Finally, the outlook and challenges to be addressed to deploy alloy anodes in commercial SIBs are also presented in this review.

2. Tin: The huge volume expansion-A problem?

Tin (Sn[50]) has been widely investigated as a potential anode for Na-ion batteries owing to its high theoretical capacity of 847 mAh g^{-1} corresponding to the fully sodiated phase of $Na_{15}Sn_4$. In addition, tin is an earth-abundant and cost-effective as well as environmentally benign metal. For the sodium-tin system, the theoretical voltage profile was calculated (Chevrier *et al.* [59]) by means of Density Functional Theory (DFT), making use of the known crystal structures from Inorganic Crystal Structure Database (ICSD). The proposed sodiation mechanism recognized the formation of intermediates such as $NaSn_5$, NaSn, Na_9Sn_4 and culminating in the fully sodiated $Na_{15}Sn_4$ phase (**Fig. 3a**). However, the subsequent experimental results of the Na-Sn system by different research groups were not in agreement with the theoretical calculations. For instance, a study of Sn-polyacrylate electrodes (Komaba *et al.* [60]) in aprotic Na cells attributed the observed four plateaus (between 0 V - 0.7 V) (**Fig. 3b**) to the phases theoretically predicted by Chevrier *et al.* One

year later in 2012, Ellis *et al.* [61] made use of Coulometry and suggested a slightly different sodiation mechanism of tin and proposed the formation of an amorphous intermediate phase during the sodiation of tin. Following this in 2017, Stratford *et al.* [62] employed ab initio random structure searching (AIRSS) and high-throughput screening from ICSD to predict the Na-Sn structures. The local and longer-range structural analysis of the phases formed were then investigated with experimental techniques including operando XRD, pair distribution function (PDF) analysis and solid-state NMR (ssNMR). The proposed mechanism for sodiation of tin is as follows (**Fig. 3c**):

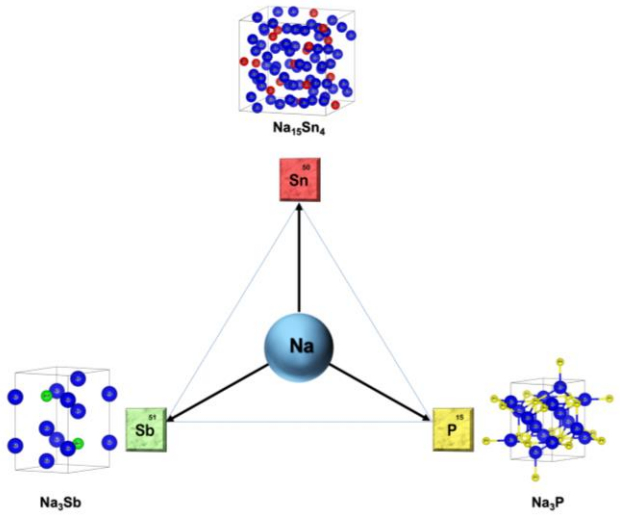

Fig. 2 Primary alloying anodes of sodium: Sn, P, Sb and the crystal structures of the sodiated phases.

Process 1: Sn→$NaSn_3$

Process 1': Sn, $NaSn_3$→ $NaSn_2$

Process 2: $NaSn_2$→ *a*-$Na_{1.2}Sn$

Process 2': *a*-$Na_{1.2}Sn$ + $NaSn_2$ → *a*-$Na_{1.2}Sn$ + expanded $Na_{1+x}Sn_2$ (solid solution)

Process 3: *a*-$Na_{1.2}Sn$ + expanded $Na_{1+x}Sn_2$ → $Na_{4.4}Sn_2$

Process 3': $Na_{4.4}Sn_2$ → $Na_{4.75}Sn_2$ (solid solution)

Process 4: $Na_{4.75}Sn_2$ → $Na_{15}Sn_4$

Process 4': $Na_{15}Sn_4$ → $Na_{15+x}Sn_4$
(*a:* amorphous)

According to Stratford and co-workers, during the initial stages of sodiation, the crystalline Sn transforms into a layered structure of approximate stoichiometry $NaSn_3$. Subsequently, $NaSn_2$ is formed, which is structurally similar to $NaSn_3$ and was predicted to be thermodynamically stable. Upon further sodiation, a crystalline to amorphous transformation was observed.

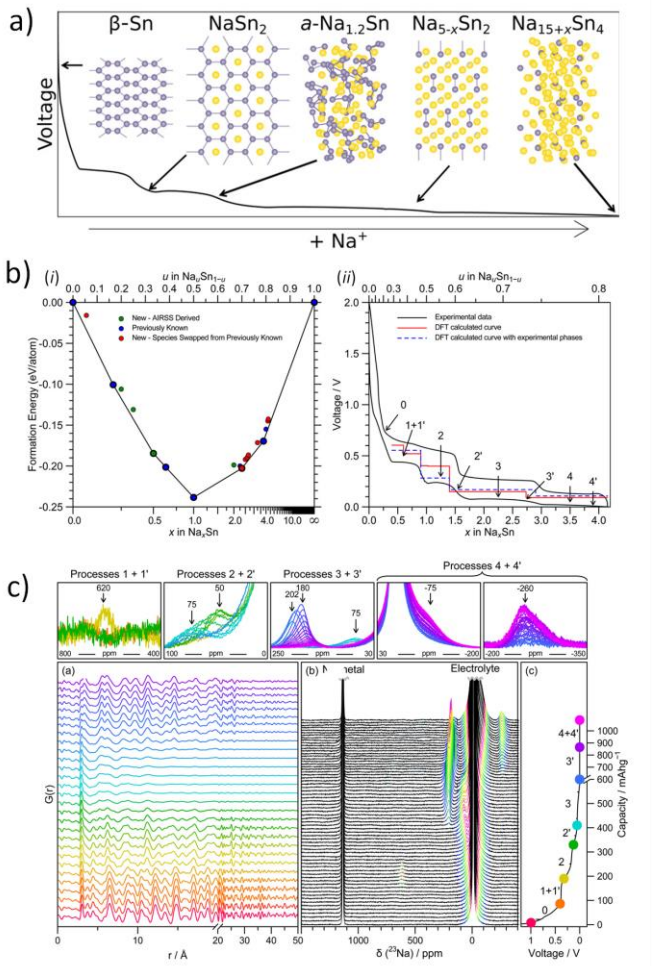

Fig. 3 (a) Sodiated phased of tin. (b) Formation enthalpy per atom *vs.* sodium concentration in the Na-Sn compound and electrochemistry data of sodium-tin cell cycled at a rate of C/20 (corresponding to achieving a capacity of 847 mAh g^{-1} in 20h) between 2 and 0.001 V (black line). (c) Operando measurements of tin *vs.* sodium showing selected PDFs and ^{23}Na-NMR spectra, and the corresponding potential profile obtained during the first discharge. (Reproduced with permission.[62] (Copyright © 2017, American Chemical Society)

From computational studies and operando PDF measurements, this amorphous phase comprised of chains of tin atoms and possess an approximate composition of $Na_{1.2}Sn$. It was observed that further reaction with sodium led to the formation of Sn-Sn dumbbells-based structures which interconvert through solid-solution mechanism. This involved the formation of $Na_{4.4}Sn_2$ followed by the formation of $Na_{5-x}Sn_2$ solid-solutions, culminating at $Na_{4.75}Sn_2$. The formation of the fully sodiated $Na_{15}Sn_4$ phase was confirmed by *ex-situ* PDF measurements (**Fig. 3c**). In addition, the possibility of incorporating excess sodium to form $Na_{15+x}Sn_4$ was deliberated as it would not require any Sn-Sn bond breaking and was confirmed by NMR measurements (**Fig. 3c**). Hence, this study clearly demonstrates the necessity to probe both short and long-range structures along with theoretical modelling to fully fathom the sodiation mechanism of alloying anodes.

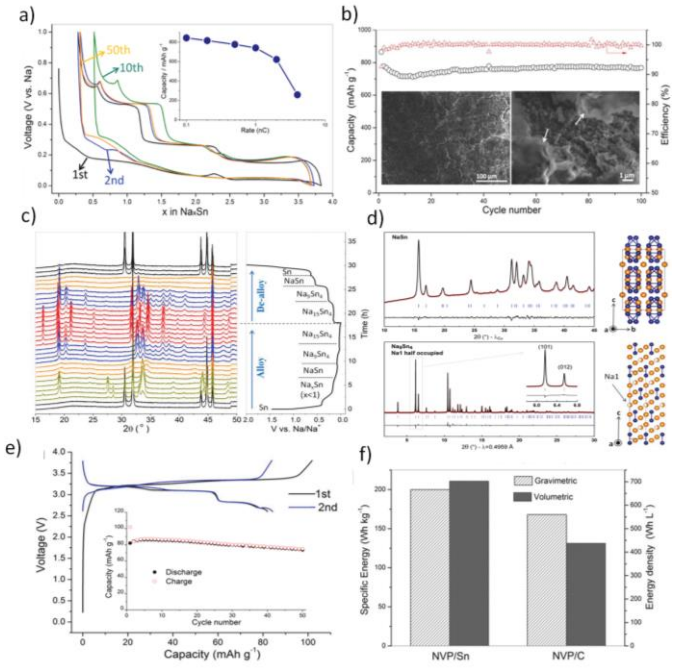

Fig. 4 (a, b) Performance of Sn electrode in the diglyme electrolyte. (c, d) *In situ*-XRD patterns during the first cycle and Rietveld refinement (Na atoms labelled orange and Sn atoms in blue. (e, f) Full cell performance of the Sn anode with hard carbon. (Reproduced with permission.[64] Copyright © 2016, John Wiley and Sons)

Importantly, bare tin undergoes huge volume changes upon sodiation and de-sodiation. A massive 420% volume change is incurred during the phase transformation of Sn to $Na_{15}Sn_4$, leading to pulverization and detachment from the current collector, causing abrupt capacity fade.[63] Hence novel strategies to mitigate the 'ill-effects' of the volume expansion of Sn need to be adopted to realize the full potential of this high-capacity anode. One such strategy was employed by Tarascon *et al.* [64] to use glyme-based electrolytes in place of the conventionally utilized carbonate-based ones. It was observed that micron-sized tin exhibited enhanced electrochemical performance in 1 M $NaPF_6$ in diethylene glycol dimethyl ether (diglyme, DGME) electrolyte (**Fig. 4a, b**). A gradual decrease in capacity was noted for the first few cycles which stabilized afterwards to deliver a capacity of 768 mAh g^{-1} after 100 cycles at a specific current of 250 mA g^{-1}. The use of micron-sized particles also aided the high coulombic efficiency of 99% achieved from the fifth cycle. The superior performance was attributed to the stable SEI formation in glyme-based electrolytes when compared to the carbonate-based systems. The formation of a stable SEI preserved the integrity of the electrode and prevented the separation of the active material from the matrix. Post-cycling examination of the electrodes cycled in glyme-based electrolyte revealed a smoother surface, while rough surface with cracks was observed on the propylene carbonate (PC) electrolyte counterpart (**Fig. 4b inset**). The composition of the SEI films was investigated by XPS and for glyme-based electrolyte, it was found to consist of both organic (RCH_2ONa) and inorganic (NaF, $NaPF_6$, Na_2O, Na_2CO_3, and phosphates) components. Similar species were found in the SEI films formed in PC electrolyte as well but in different proportions and was attributed to the higher solubility of sodium carbonates and oxides in PC. The in situ-XRD studies (**Fig. 4c**) revealed the phase transitions occurring during the alloying reactions. Various Na_xSn phases were identified as the alloying reaction of Sn and Na proceeds, culminating in $Na_{15}Sn_4$ upon full sodiation of Sn (**Fig. 4d**). Furthermore, the viability of micron-sized tin negative electrode in glyme-based electrolyte was further demonstrated in a full-cell configuration with $Na_3V_2(PO_4)_3$ as positive electrode (**Fig. 4e**). The full-cell exhibited 102 mAh g^{-1} of charge capacity and 83 mAh g^{-1} discharge capacity in the first cycle when cycled at C/5 rate at an average voltage of 3 V. The full-cell retained 90% of the initial capacity after 50 cycles. An energy density of 200 Wh kg^{-1} (mass of active materials in cathode and anode accounted) is achieved in the 50th cycle. When compared with an NVP-carbon full cell, the NVP-tin full cell exhibited 19% higher gravimetric and 61% higher volumetric energy densities (**Fig. 4f**). Further studies on the long-term stability and the cost of glyme-based electrolyte systems are called for to advance tin-based high-performance anodes for SIBs.

Another significant approach was the deployment of porous tin anode fabricated by a phase-inversion technique. The porous structure was able to mitigate the ill-effects of the volume expansion as evident from the high reversible capacity of 524 mAh g^{-1} retained after 500 cycles and a high Coulombic efficiency of ~99%.[65] Hence, the use of Sn as active material in SIBs should consider the huge volume changes occurring during the sodiation process. **Table 1** summarizes various strategies adopted to overcome the cycling instability issue in tin anode including structural modifications, incorporation of active/inactive buffer matrix, Sn-M intermetallics among others. By adopting these strategies, the electrode disintegration resulting from the volume expansion can be controlled and the cycling stability can be enhanced.

3. Antimony: novel strategies to improve the cycling performance

Antimony (Sb[51]) is one of the most promising alloying anodes for SIBs as it offers a high theoretical sodiation capacity of 660 mAh g^{-1} corresponding to the fully sodiated Na_3Sb phase. Understanding the sodium storage mechanism of antimony can help to devise efficient strategies to improve its electrochemical performance. In the past, various groups have investigated the sodiation mechanism of antimony. Among them, the sodiation of thin films of antimony was investigated by means of ^{121}Sb Mössbauer spectroscopy (Baggetto *et al.* [80]). The formation of an amorphous intermediate phase resembling NaSb was suggested, which was followed by the formation of crystalline Na_3Sb phase upon full sodiation. Later, studies by Monconduit *et al.* [81] reported the buffering of the strain by an intermediate amorphous phase leading to the improved sodiation performance of micrometric antimony. It was only recently by Allan *et al.* [82] using coupled PDF analysis and solid-state NMR to further understand the alloying mechanism of antimony in SIBs

(**Fig. 5**). The previously uncharacterized intermediate phases have been identified in the study and the (de-)sodiation mechanism was explained as follows (**Fig. 5a, b**):

Table 1. Comparison of performance of tin-based anodes in recent literature

Sn-based anodes- morphology/ structure	Synthesis method	Sodiation capacity (second cycle)	Capacity retention (cycle life)	Potential Window (V *vs.* Na)
Porous tin[65]	Phase-inversion technique	659 mAh g^{-1} @423.5 mA g^{-1}	~77% (500 cycles)	0.001-1
Tin nanoparticles encapsulated in graphene backboned carbonaceous foams[66]	Hydrogen-assisted thermal reduction	~600 mAh g^{-1} @400 mA g^{-1}	~84% (500 cycles)	0.01-2
Sn nanoparticles@nitrogen-doped carbon nanofiber composites[67]	Electrospinning	~690 mAh g^{-1} @84.7 mA g^{-1}	~87% (200 cycles)	0-2.5
Sn coated reduced graphene oxide-graphene composite[68]	Camera flash reduction	~690 mAh g^{-1} @423.5 mA g^{-1}	~72% (100 cycles)	0.01-2
Yolk–shell carbon encapsulated tin[69]	Hydrothermal synthesis	~500 mAh g^{-1} @100 mA g^{-1}	~80% (100 cycles)	0.02-3
Multi-layered 2D Sn Nano-dendrites[70]	Electrodeposition	~783 mAh g^{-1} @100 mA g^{-1}	~96% (300 cycles)	0.001-0.65
Sn_4P_3 nanotops[71]	Solution-based synthesis	~600 mAh g^{-1} @50 mA g^{-1}	~83% (80 cycles)	0.01-2
Sn_4P_3/Reduced graphene oxide hybrids[72]	Solution-based synthesis	~900 mAh g^{-1} @100 mA g^{-1}	~77% (100 cycles)	0.01-3
Sn_4P_3/Graphene nanocomposite[73]	Mechanochemical synthesis	~600 mAh g^{-1} @1 A g^{-1}	~99% (1000 cycles	0-2
Intermetallics of Sn				
SnTe-carbon composite[74]	Solid state synthesis	~541 mAh g^{-1} @50 mA g^{-1}	~99.1% (100 cycles)	0-2.5
$MnSn_2$ alloy[75]	Ball milling method	~400 mAh g^{-1} @18.35 mA g^{-1}	~89.8% (50 cycles)	0-1.5
$FeSn_2$-graphite composite[76]	Solvothermal and ball milling method	~450 mAh g^{-1} @100 mA g^{-1}	~83% (200 cycles)	0.005-2
SnSe Nanoparticles Confined in Graphene[77]	Ball milling method	~410 mAh g^{-1} @1 A g^{-1}	~95% (120 cycles)	0.01-2
$SnSe_2$ 2D Anodes[78]	Hydrothermal method	~600 mAh g^{-1} @100 mA g^{-1}	~88% (100 cycles)	0.005-2.5
SnCo/carbon composite[79]	Solution-based synthesis	~300 mAh g^{-1} @100 mA g^{-1}	~87% (120 cycles)	0.1-2

1st Sodiation: c-Sb → a-$Na_{3-x}Sb$ + c-Na_3Sb → c-Na_3Sb.

1st Desodiation: c-Na_3Sb → a-$Na_{1.7}Sb$ → a-$Na_{1.0}Sb$ → a-$Na_{1.0}Sb$ + c-Sb

2nd Sodiation: a-$Na_{1.0}Sb$ + c-Sb → a-$Na_{1.7}Sb$ + c-Sb → a-$Na_{1.7}Sb$ + a-$Na_{3-x}Sb$ →a-$Na_{3-x}Sb$ → c-Na_3Sb

(c: crystalline a: amorphous)

Briefly, the sodiation of antimony was observed to proceed through two intermediate amorphous phases $Na_{3-x}Sb$ and $Na_{1.7}Sb$, which alleviated the strain associated with multiple phase transitions. Upon full sodiation, the electrode composition comprised of amorphous and crystalline antimony networks. These components had different reaction voltages aiding a sequential reaction profile (**Fig. 5c**) with the inactive component accommodating the strains generated during the sodiation of the active components. *Ex-situ* ^{23}Na NMR and PDF analyses (**Fig. 5d**) indicated the formation of amorphous $Na_{3-x}Sb$

phases during the initial sodiation of Sb. The absence of NaSb phase during sodiation or desodiation of Sb at room temperature was ascribed to the lack of mobility of Sb within the Na_xSb phases. Similarly, the formation of under-sodiated a-$Na_{3-x}Sb$ was attributed to the difficulties in nucleating Na_3Sb where the breaking of Sb-Sb bonds is required. On the other hand, the good rate performance of antimony was attributed to the high sodium mobility in the crystalline Na_3Sb phase aiding facile structural transformations during sodium movement in and out of the structure.

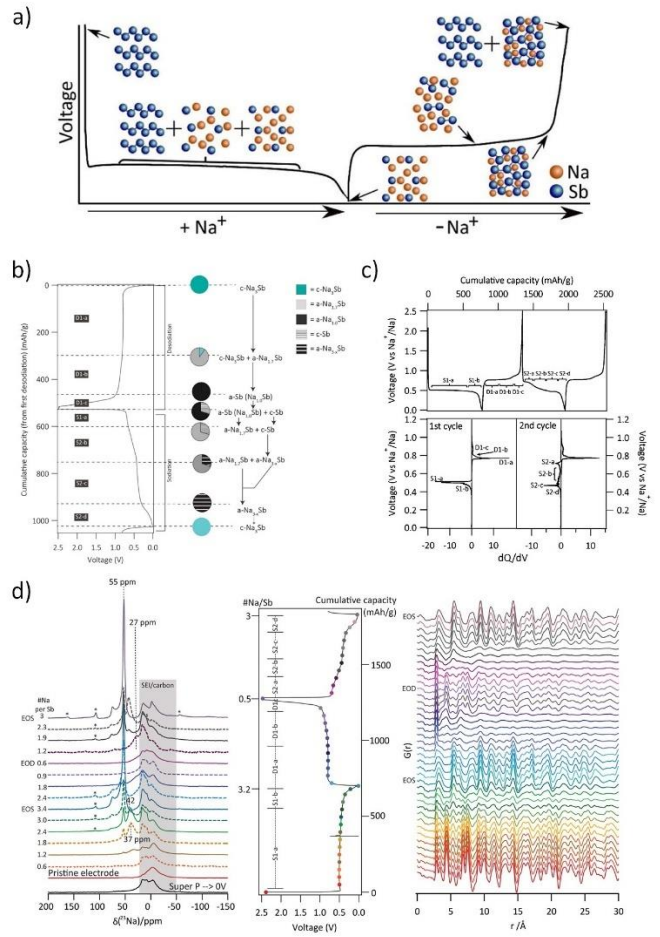

Fig. 5 (a) Structural changes to antimony during sodiation/de-sodiation process. (b) PDF and NMR derived mechanisms of (de) sodiation of antimony. (c) (De)sodiation curves and corresponding dQ/dV plots for 1st and 2nd cycles at C/20 rate. (d) *Ex situ* ^{23}Na-NMR and PDF spectra of the cycled antimony electrodes. (Reproduced with permission.[82] Copyright © 2016, American Chemical Society)

However, antimony undergoes a volume change of ~293% during the alloying reaction with Na to form Na_3Sb.[83] This induces pulverisation of the Sb particles and the loss of electrical contact with the conducting matrix. Moreover, the freshly formed Sb surface when exposed to the electrolyte can result in the formation of new SEI, causing further irreversible capacity losses. One of the approaches employed to improve the cycling stability is to make use of an effective matrix to contain the Sb particles. In this regard, Wu *et al.* [84] investigated the performance of Sb-carbon (Sb-C) nanofibers synthesized through a facile electrospinning technique (**Fig. 6a, b**). The nanofibers delivered nearly 631 mAh g^{-1} at C/15 rate and retained ~90% of the capacity after 400 cycles (**Fig. 6c**). The superior performance of the Sb-C nanofibers was attributed to the well-dispersed antimony nanoparticles in the unique nanofiber structure (**Fig. 6b**) and the conducting and buffering effect of the supporting carbon matrix during Na insertion and extraction.

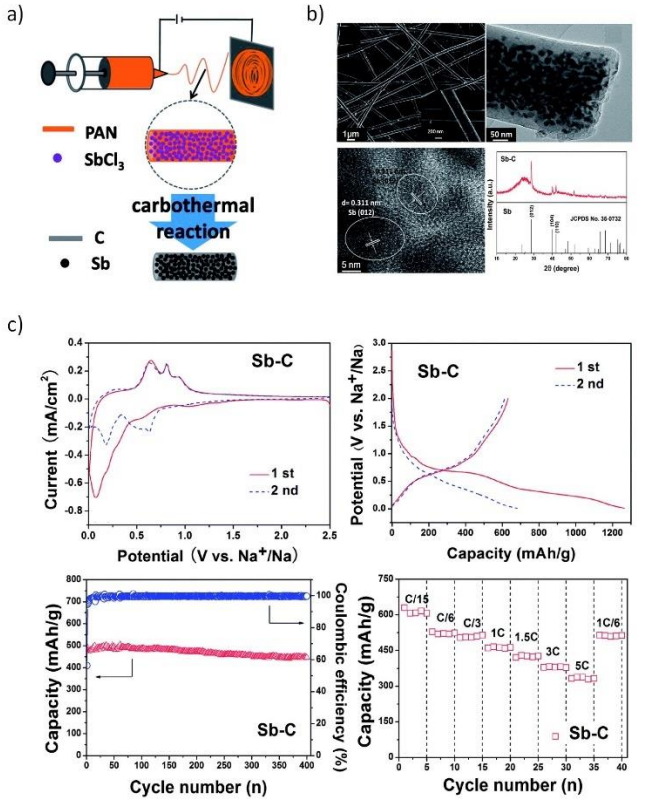

Fig. 6 Sb-C Nanofibers. (a) Schematic illustration of the synthesis process; (b) SEM, TEM images and XRD pattern of the Sb-C nanofibers. (c) Electrochemical performance of the Sb-C nanofibers. (Reproduced with permission.[84] Copyright © 2014, The Royal Society of Chemistry)

Recently, Liu and group proposed a galvanic replacement technique to synthesize hollow Sb-C yolk-shell spheres (**Fig. 7a**) that delivered superior sodium storage performance.[85] The void space in the Sb yolk allowed volume expansion during the sodium storage and the carbon shell facilitated a stable SEI formation. The yolk-shell spheres delivered a reversible capacity of 280 mAh g^{-1} at 1 A g^{-1} after 200 cycles (**Fig. 7b**). Similarly, free-standing metallic Sb nanosheets were synthesized from the grey Sb allotrope (Gu *et al.* [86]) by means of a liquid-phase exfoliation technique in an isopropyl alcohol-sodium hydroxide solution. The obtained Sb nanosheets were of ~4 nm thickness with graphene-like foldable features and large aspect ratios (**Fig. 7c**). Furthermore, hybrid sheets of graphene and Sb nanosheets with tuneable densities were also fabricated and they demonstrated excellent electrochemical

performance with a reversible volumetric capacity of 1126 mAh cm^{-3} (**Fig. 7d)**.

Another noteworthy strategy to overcome the capacity decay arising from volume changes to the Sb anode was illustrated by Gao *et al.* [87] by employing a cross-linked chitosan polymer network binder. The Sb particles were immobilized in the cross-linked chitosan network which suppressed the adverse mechanical effects from huge volume expansion and thereby enhanced the electrochemical performance. The electrode exhibited a capacity of ~555 mAh g^{-1} at 1C rate over 100 cycles with 96.5% capacity retention and ~99% coulombic efficiency. Furthermore, the cross-linked chitosan binder outclassed the conventional CMC and PVDF binders in terms of cycling performance.

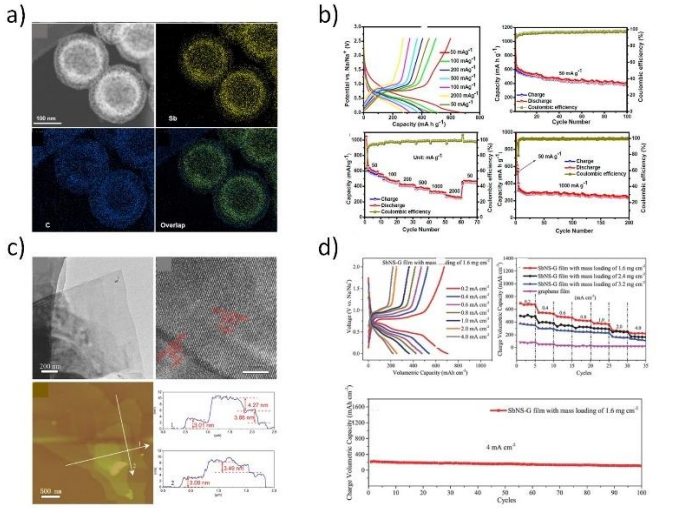

Fig. 7 (a) Dark-field TEM micrographs and elemental maps of Sb-C yolk-shell particles. (b) Sodium-storage performance of the yolk-shell particles. (Reproduced with permission.[85] Copyright © 2017, American Chemical Society). (c) TEM and AFM images of liquid-phase exfoliated Sb nanosheets of thickness 3.0 to 4.3 nm and their sodium-storage performance (d). (Reproduced with permission.[86] Copyright © 2017, John Wiley and Sons)

While the formation of amorphous phases and fewer phase transitions during the sodiation of Sb enables better performance when compared to Sn, structural modification to Sb and the application of Sb-M intermetallics are other strategies to improve the electrochemical performance of Sb anodes. **Table 2** summarizes the novel strategies employed in the recent past by various research groups.

4. Phosphorous: confronting the poor conductivity and cycling instability

Among others, probably elemental phosphorus (P[15]) has the highest theoretical sodiation capacity of all known materials (2596 mAh g^{-1} corresponding to the Na_3P sodiated phase).[103] This is even higher than the electrochemical capacity of metallic Na (1166 mAh g^{-1}). Pioneering studies on the sodiation/lithiation processes in phosphorous was carried out by Mayo and co-workers[104] through a first-principles structure prediction study combined with NMR calculations. The local environment evolution of phosphorous during sodiation/lithiation was predicted by calculating average voltage profiles, energy density of states and NMR chemical shielding of the ground state phases (**Fig. 8a-c**). A new phase, Na_5P_4 with C2/m symmetry was predicted to exhibit a layered structure comprising of sodium sheets separated by four-bounded in-plane phosphorus chains. The new phase is calculated to be thermodynamically stable and was further confirmed by the phonon dispersion calculations- indicating a possibility to be observed in future experimental studies. The volume change during the formation of various Na_xP phases with respect to black phosphorus was also calculated using DFT-PBE lattice parameters (**Table 3**).

When compared to tin and antimony, phosphorus anode suffers from inherently poor conductivity in addition to its enormous volume changes during (de-)sodiation reactions. To overcome this problem, Zhang *et al.* [105] introduced an innovative flexible paper made of nitrogen-doped graphene and amorphous phosphorus as the anode (**Fig. 8d**). The restructured anode exhibited excellent structural integrity and demonstrated a remarkable capacity of ~809 mAh g^{-1} at a high specific current of 1500 mA g^{-1} (**Fig. 8e**). The restructured anode also exhibited good capacity retention of >85% after 350 cycles at 800 mA g^{-1}. Furthermore, the sodiation process was investigated via in-situ HRTEM studies (**Fig. 8f**). The superior electrochemical performance of the restructured anode was attributed to the relatively smaller volume change of amorphous phosphorus over the crystalline phase, as well as the excellent electrical conductivity and robustness of the N-doped graphene networks which also effectively buffers the volume changes in the electrode.

To further improve the electrochemical performance of phosphorous-based anodes, it is crucial to investigate the formation and the stability of the solid-electrolyte interphase. In this regard, Dahbi and group[106] probed the evolution of the electrode/electrolyte interphase of black phosphorus negative electrode in Na cells. The formation of the SEI in $NaPF_6$ electrolyte with fluoroethylene carbonate (FEC) and vinylene carbonate (VC) additives were investigated using hard X-ray photoelectron spectroscopy (HAXPES) and time-of-flight secondary ion mass spectroscopy (TOF-SIMS). The SEI layer was found to comprise mainly of inorganic species originating from the decomposition of the electrolyte solvents and additives. The accumulation of organic carbonate species was found near the electrode surface and in addition, inorganic salt decomposition species were also observed. The sodiated phase Na_3P is found to be highly reactive- causing severe electrolyte decomposition leading to rapid capacity fading. Longer cycling life and better reversibility was achieved for 1M $NaPF_6$ in EC/DEC electrolyte with VC additive (**Fig. 9**). The addition of FEC and VC additives in the electrolyte resulted in the formation of a stable surface layer via decomposition and polymerization of FEC (**Fig. 9b**) and VC (**Fig. 9c**) which passivated the electrode and suppressed the

electrolyte decomposition. Further studies are called for to investigate VC additives to realize SIBs with long calendar life.

Recently, hollow nanospheres of red phosphorous (HPN) with porous shells and controlled diameters were fabricated by Zhou *et al.* [107] through a solvothermal technique and investigated their performance as LIB and SIB anodes (**Fig. 10a**). The HPN anodes demonstrated excellent electrochemical performance as SIB anode, retaining a high reversible capacity of ~969 mAh g^{-1} at 1C (2.6 A g^{-1}) (**Fig. 10b**). The hollow nanospheres maintained their morphology even after cycling-suggesting the capability of the spheres to accommodate the volume-expansion induced strains.

In addition to the volume expansion issue, the intrinsic low conductivity of pure phosphorus requires a conductive matrix, mainly carbon or metallic-based to improve the electrochemical performance. Moreover, the high reactivity of the sodiated Na_3P phase also requires tuning the solid-electrolyte interphase to minimize the subsequent electrolyte decomposition. Various strategies such as carbon-phosphorous composites and metallic phosphides were investigated as negative electrodes for SIBs and are summarized in **Table 4**.

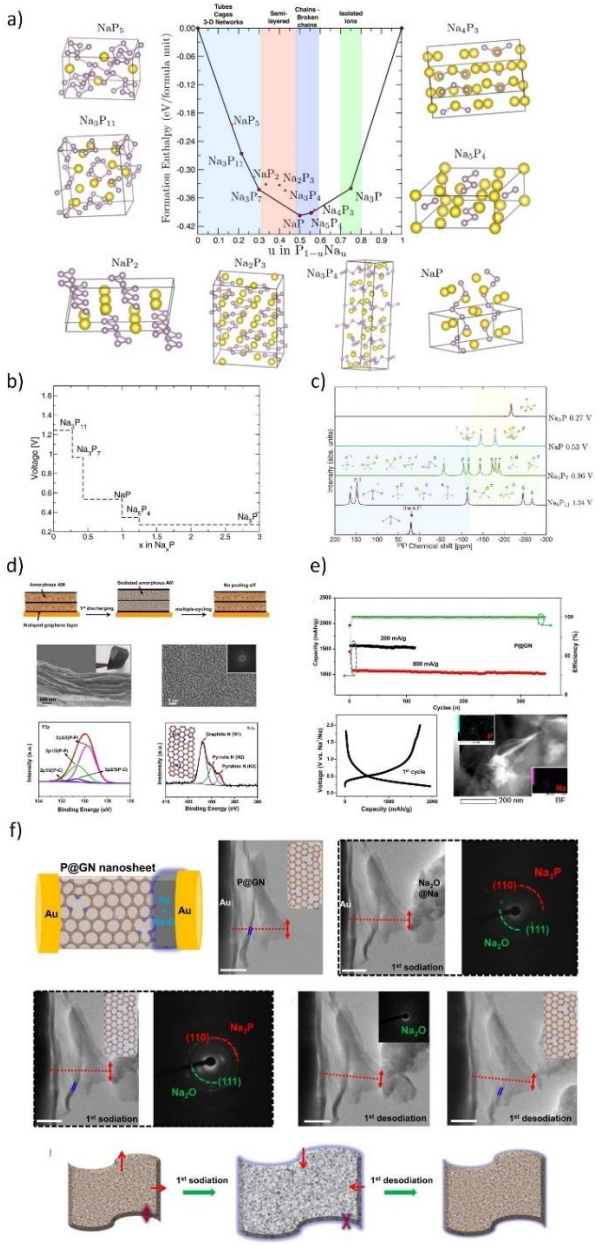

Fig. 8 (a) Formation enthalpy per atom versus the fractional sodium concentration in the Na-P compound. (b) Calculated average voltages for the Na-P phases. (c) Calculated ^{31}P-NMR Chemical shifts for various Na-P phases. (Reproduced with permission.[104] Copyright © 2017 American Chemical Society). (d) Amorphous P-graphene anode with "butter-bread" structure. (e) Galvanostatic cycling performance and potential profiles (f). *In situ*-HRTEM Sodiation and the time dependant TEM images with SAED patterns. (Reproduced with permission. [105] Copyright © 2016, American Chemical Society)

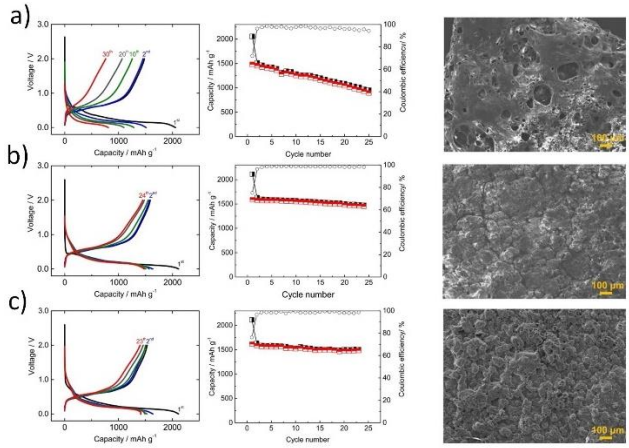

Fig. 9 Electrochemical properties of black P/polyacrylonitrile electrodes in Na-cells. Potential profiles and reversible capacity of phosphorous electrodes in 1 M $NaPF_6$/EC/DEC/electrolyte: (a) without additive, (b) with Fluoroethylene carbonate additive, and (c) with vinylene carbonate additive and corresponding SEM images of cycled electrodes. (Reproduced with permission.[106] Copyright © 2016, American Chemical Society)

Table 2. Comparison of performance of antimony-based anodes in recent literature

Sb-based anodes-morphology/ structure	Synthesis method	Sodiation capacity (second cycle)	Capacity retention (cycle life)	Potential window (V *vs.* Na)
Antimony Hollow Nanospheres[85]	Galvanic replacement reaction	~627 mAh g^{-1} @400 mA g^{-1}	~99.6% (50 cycles)	0.01-2
Cypress leaf-like Sb[88]	Chemical replacement reaction	~640 mAh g^{-1} @100 mA g^{-1}	~98% (120 cycles)	0.01-2
Sb nanoparticles anchored on carbon nanofibers networks[89]	Pyrolysis combined with $NaBH_4$ reduction	~542 mAh g^{-1} @100 mA g^{-1}	~96.7% (100 cycles)	0.01-2
3-D gradational Sb–NiSb–Ni heterostructures[90]	Pulsed electrodeposition	650 mAh g^{-1} @66 mA g^{-1}	~62% (300 cycles)	0.01-1.5
Spherical nano Sb-carbon composite[91]	Spray pyrolysis	~435 mAh g^{-1} @100 mA g^{-1}	~88.5% (500 cycles)	0.01-2
Sb Nanospheres on Graphene[92]	Solution-based synthesis	~460 mAh g^{-1} @250 mA g^{-1}	~97% (200 cycles)	0.01-2
Sb/C Fibers[93]	Electrospinning	~420 mAh g^{-1} @100 mA g^{-1}	~83% (300 cycles)	0-2
Sb nanodots embedded 2D carbon nanosheets[94]	Solution-based top-down strategy	~461 mAh g^{-1} @100 mA g^{-1}	~82% (250 cycles)	0.005-2
Intermetallics of Sb				
SnSb nanocrystals[95]	One-pot reduction	~400 mAh g^{-1} @660 mA g^{-1}	~87% (100 cycles)	0.02-1.5
Reduced Graphene Oxide/SnSb nanocomposites[96]	Hydrothermal reaction	~450 mAh g^{-1} @100 mA g^{-1}	~87% (80 cycles)	0.001-2.5
Nanoporous Bi_2Sb_6[97]	Chemical dealloying process	~562 mAh g^{-1} @200 mA g^{-1}	~76% (100 cycles)	0.01-2
Cu_2Sb Nanoparticles integrated on Cu Foil[98]	Replacement reaction	~400 mAh g^{-1} @660 mA g^{-1}	~98% (200 cycles)	0.05-2
Ni–Sb intermetallic hollow nanospheres[99]	Solvothermal and ball milling method	~600 mAh g^{-1} @66 mA g^{-1}	~83% (70 cycles)	0.01-2
Fe-Sb ribbons[100]	Melt-spinning technique	~466 mAh g^{-1} @50 mA g^{-1}	~95% (80 cycles)	0.005-2

Zn_4Sb_3 intermetallic nanowires[101]	Self-catalysis using reactive vapor transport	~350 mAh g^{-1} @41.4 mA g^{-1}	~86% (200 cycles)	0.01-2
Zn_4Sb_3 Films[102]	Electrodeposition	~400 mAh g^{-1} @97.2 mA g^{-1}	~90% (250 cycles)	0.1-1.2

Table 3. Volume change during the formation of various Na_xP phases

x in Na_xP	Volume per P atom (Å^3)	Volume change (%)
0	19.28	-
3/11	29.98	55.50
3/7	36.25	88.04
1	42.33	119.58
5/4	49.37	156.10
3	94.89	392.25

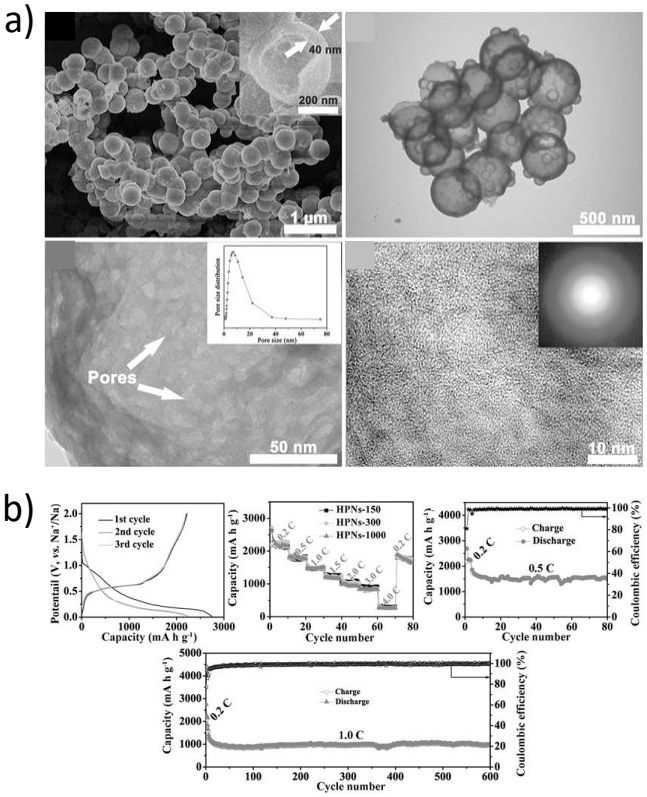

Fig. 10 (a) SEM and TEM images of the prepared hollow nanospheres (HPNs); (b) Cycling stability and rate performance of HPNs *vs.* Sodium. (Reproduced with permission. [107] Copyright © 2017, John Wiley and Sons).

5. Progress on Bismuth, Germanium and Silicon based anodes

In addition to tin, antimony and phosphorus, elements such as Bi, Ge and Si are also known to form various Na_xM (M=Bi, Ge, Si) phases at ambient temperatures. For instance, Bismuth forms NaBi and Na_3Bi at room temperatures and has a theoretical capacity of 385 mAh g^{-1} corresponding to the fully sodiated Na_3Bi phase.[118] However, the reports on sodiation mechanism of Bi are quite inconsistent. The in operando XRD studies (Ellis *et al.* [119]) on sputtered Bi anode revealed the sodiation to proceed according to the Na-Bi phase diagram (**Fig. 11a, b)** with the formation of NaBi and terminating in the fully sodiated Na_3Bi phase. On the other hand, Sun et al. [120] investigated graphene wrapped Bi nanoparticles and concluded that the large interlayer spacing along the *c*-axis (*d* (003) =3.95 Å) facilitates intercalation of Na-ions *vs*. alloying and supported the claim by the ex-situ XRD measurements as well as DFT calculations.

Table 4. Comparison of performance of phosphorous-based anodes in recent literature.

P-based anodes- morphology/ structure	Synthesis method	Sodiation capacity (second cycle)	Capacity retention (cycle life)	Potential Window (V *vs.* Na)
Integrated Carbon/Red Phosphorus/Graphene Aerogel 3D Architecture[108]	Vapour-Redistribution technique	~2086 mAh g^{-1} @260 mA g^{-1}	~89.5% (100 cycles)	0.01-2

Amorphous red phosphorus/carbon composite[109]	High energy ball-milling	~1400 mAh g^{-1} @250 mA g^{-1}	~71% (80 cycles)	0.01-2
Amorphous red phosphorus/carbon composite[110]	High energy ball-milling	~1890 mAh g^{-1} @143 mA g^{-1}	~93% (30 cycles)	0-1.5
Phosphorene-graphene hybrid[111]	Solution-based synthesis	~1450 mAh g^{-1} @8 A g^{-1}	~84% (100 cycles)	0.02-1.5
Red Phosphorus Nanodots on Reduced Graphene Oxide[112]	Physical vapor deposition	~1074.5mAh g^{-1} @1593.9 mA g^{-1}	~86.6% (100 cycles)	0.01-1.75
Red P-TiP_2–C Nanocomposite[113]	High energy mechanical milling	~755 mAh g^{-1} @200 mA g^{-1}	~80.4% (100 cycles)	0-1.5
FeP[114]	Ball milling	~465 mAh g^{-1} @50 mA g^{-1}	~69% (60 cycles)	0-1.5
NiP_3 [115]	Ball milling and ceramic routes	~1000 mAh g^{-1} @159.1 mA g^{-1}	~81% (20 cycles)	0-2.5
CoP [116]	Ball milling	~470 mAh g^{-1} @100 mA g^{-1}	~65.5% (25 cycles)	0-1.5
SiP_2 [117]	Ball milling	~750 mAh g^{-1} @890 mA g^{-1}	~71% (15 cycles)	0-1.5

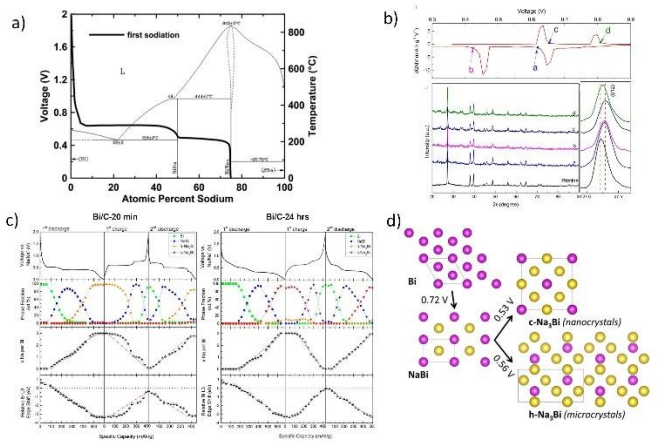

Fig. 11 (a) Voltage curve of the first sodiation half-cycle of sputtered bismuth overlaid onto the Na-Bi binary phase diagram. (Reproduced with permission. [118,119] Copyright © 2014, The Electrochemical Society). (b) Differential profiles and ex-situ XRD patterns of Bi/graphene nanocomposite at different charge and discharge status. (Reproduced with permission.[120] Copyright © 2015, Elsevier) (c) Voltage profiles, Na-Bi phase fractions and the relative edge shifts. (d) Illustration of the different structural and electrochemical pathways in the Na-Bi system. (Reproduced with permission. [121], Copyright © 2016, American Chemical Society)

Recently, Sottmann and co-workers[121] elucidated the influence of crystallite size of Bi on the sodiation mechanism. It was found that nano crystallite size alters the Na-Bi system and influences the electrochemical performances, including cycling stability. From in operando synchrotron XRD/XAS studies, it was concluded that nano-sized Bi forms the cubic Na_3Bi phase upon sodiation whereas the micro-sized Bi forms the hexagonal Na_3Bi phase (**Fig. 11c, d**). This difference in the reaction pathway is said to impart the difference in electrochemical performance of nano and micro Bi, with the former exhibiting superior cycling stability over the latter.

According to the Na-Si phase diagram, Silicon is reported to form four intermetallic phases with Na: NaSi, $NaSi_2$, Na_4Si_{23}, $NaSi_{94}$.[122] The NaSi phase corresponds to a theoretical capacity of 954 mAh g^{-1}. However, previous studies by Komaba *et al.* [60] and Ellis *et al.* [119] found that Si is electrochemically inactive at room temperature or even upto 60 °C. It was only recently Zhao and co-workers[123] reported Si-carbon nanocomposite obtained via ball milling to deliver ~300 mAh g^{-1} at a specific current of 100 mA g^{-1} for 100 cycles in the potential window of 0.01-3 V *vs.* Na. Similarly, the sodiation behaviour of amorphous silicon prepared through various synthetic routes including chemical delithiation, high-energy ball milling and mechanical fusion method was investigated by Lim and others.[124]The mechanically fused Si-Sn composite exhibited a stable capacity of ~150 mAh g^{-1} at 36.25 mA g^{-1} for over 100 cycles. Lately, the sodiation of crystalline silicon anode was examined via in operando Raman and XRD analysis by Zhang and group (**Fig. 12**).[125] The crystalline Si anode was found to undergo an irreversible crystal structure transformation during the first sodiation/desodiation process leading to an irreversible amorphous Si phase. During the subsequent cycles, the amorphous phase was found to reversibly react with sodium. However, pure nano-sized crystalline Si still exhibited poor cycling stability, and this was attributed to the volume changes during sodium insertion/extraction leading to structural degradation and instability. To improve the cycling stability, a bamboo rattle type Si/C film with a well-defined yolk-shell architecture was fabricated via electrospinning and exhibited ultrafast sodium storage with high capacity and cycling stability (**Fig. 12a-c**). The poor conductivity and inferior structural stability of amorphous silicon was mitigated by the 3D carbon framework which also imparts flexibility and mechanical integrity to the anode, resulting in the excellent electrochemical performance. The

potential profiles (**Fig. 12 d**) indicate the typical alloying reaction during the initial (de-)sodiation processes and the capacitive behaviour in the subsequent cycles. Moreover, the operando XRD investigation of micro sized crystalline silicon (**Fig. 12e**) revealed the absence of structural changes or reversible reactions and suggested the strong dependence of particle size and surface area on the electrochemical performance of crystalline silicon.

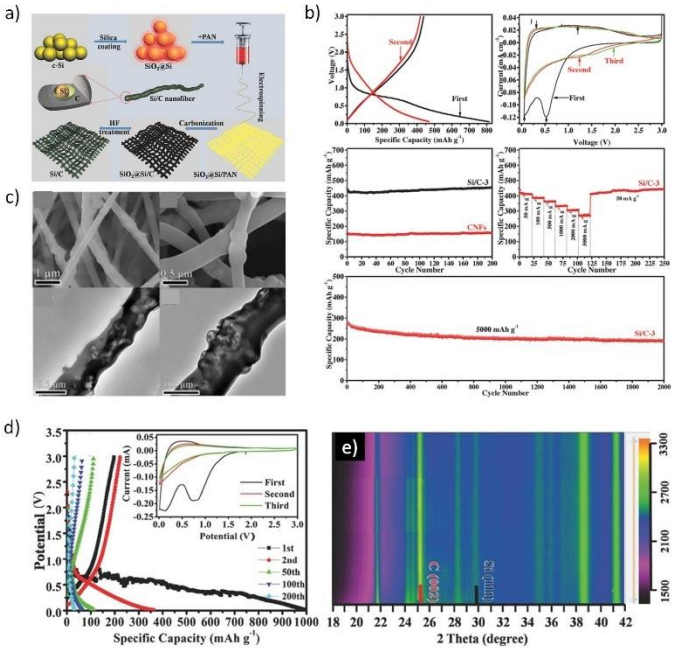

Fig. 12 (a) Illustration of Si-C composite design. (b) Electrochemical performance of Si-C composite as sodium-ion battery anode. (c) SEM and TEM images of the bamboo-rattle like Si-C architecture. (d) Potential profiles of nano sized Si and (e) Operando XRD plot of micro sized Si *vs.* sodium. (Reproduced with permission. [125] Copyright © 2016, John Wiley and Sons)

Germanium has received great attention in the recent years as a potential candidate for electrochemical energy storage applications.[126] Ge has a theoretical sodiation capacity of 369 mAh g^{-1} corresponding to NaGe phase upon full sodiation. The first report on Ge thin germanium thin film anodes for SIBs was by Baggetto *et al.* [127]. A reversible capacity of ~350 mAh g^{-1} was obtained for the thin film electrodes but the capacity was found to fade after 15 cycles due to the volume expansion. The capacity retention was improved considerably by using FEC additive which facilitated the formation of thinner SEI. The thin film electrodes also demonstrated excellent rate capability retaining close to 220 mAh g^{-1} at 170 C and 110 mAh g^{-1} at 340 C. It was recently demonstrated by different research groups that the high diffusion barrier for Na ions in crystalline Ge could be considerably lowered by making use of amorphous Ge with high defect density.[128-130]Recently, real time *in-situ* transmission electron microscopy (TEM) (**Fig. 13a, b**) was employed to investigate (de)sodiation processes in Ge nanowires (Lu and co-workers[131]). It was found that only amorphous Ge nanowires undergo sodiation/desodiation and the crystalline Ge nanowires were inactive. Upon sodiation, the amorphous nanowires exhibited nearly 300% volume expansion corresponding to $Na_{1.6}Ge$, indicating a higher capacity than NaGe. The desodiation of nanowires led to the formation of pores, which disappear when the nanowire was again sodiated (**Fig. 13b**). Similarly, Ge nanoparticles encapsulated in hollow carbon boxes were synthesized by Li and co-workers by a carbothermal reaction route (**Fig. 13c**).[132] After 500 cycles at a specific current of 100 mA g^{-1}, the anode displayed a remarkable sodium storage capacity of 346 mAh g^{-1} (**Fig. 13d**). The enhanced electrochemical performance is attributed to the internal void space of the carbon boxes which accommodate the volume expansion as well as the interconnectivity of the carbon shell that imparts good electrical conductivity to the electrode. Further studies are necessary to elucidate the sodiation mechanism in amorphous Ge particles and the cycling performance to facilitate their application in practical SIBs.

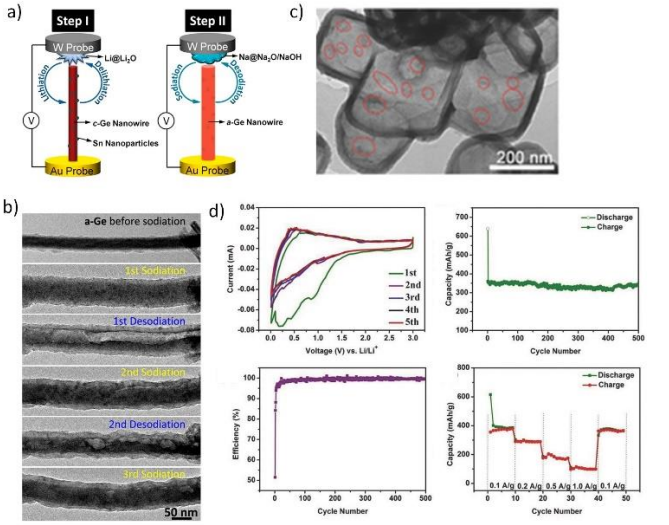

Fig. 13 (a) Illustration of the *in situ* TEM procedure on Ge nanowire. (b) Structural evolution of Ge nanowire during (de) sodiation cycles. (Reproduced with permission.[131] Copyright © 2016, American Chemical Society). (c) Hollow carbon boxes encapsulating Ge and the electrochemical performance is presented in (d). (Reproduced with permission.[132] Copyright © 2017 John Wiley and Sons.)

6. Mitigating the challenges of alloying anodes

One of the primary challenges hindering the deployment of alloying anodes in practical sodium-ion batteries is their cycling instability induced by the huge volume expansion. In the previous sections we have expounded the sodiation mechanisms in alloying anodes-the knowledge of which can help devise efficient sodiation pathways thereby improving the electrochemical performance. The various strategies adopted to improve the performance of alloying anodes can be summarized as follows:

6.1 Engineering the active materials

Structural and morphological modifications of the active material is one of the widely adopted strategies to alleviate the problem of particle pulverization during (de)sodiation

reactions. Making use of porous/hollow active materials was found to improve the particle integrity during the cycling process and enhanced the calendar life. The approach seems promising in terms of the electrochemical performance while the scale-up of the synthesis techniques is a concern to be addressed. Another approach was to embed the active material in a carbon matrix including the *in-situ* encapsulation during the synthesis or post-processing via carbonization or ball-milling. The carbon matrix was found to improve the conductivity as well as buffer the volume changes during electrochemical cycling. Again, the low tap-density of carbon should be considered, and the carbon content should be minimized to avoid any penalty in the volumetric energy density. Recently, nano-engineering of active materials including the utilization of 2D nanosheets of alloying anodes (antimonene, phosphorene) has gained significant attention. The 2D nanosheets were found to effectively buffer the volume changes and could be a promising approach if cost-effective and scalable synthesis processes are devised.

6.2 Intermetallics to improve the cycling stability

Recently, intermetallics of tin, antimony and phosphorous (M-Sn/Sb/P) have gained interest because of their superior electrochemical performance when compared to the bare alloying elements. Most of these intermetallics can be synthesized by scalable, industrially-viable techniques including ball-milling, solid state synthesis and melt-spinning to name a few. The accompanying element 'M' in the intermetallic could be active or inactive towards sodium storage. For instance, in SnSb, both Sn and Sb are active while in $FeSn_2$ only Sn is electrochemically active. The component 'M' whether active or inactive, still plays a vital role to enhance the performance. In most cases, during the first sodiation process of the intermetallic anode, the component 'M' is extracted out and forms a matrix for the sodiated active component. The enhanced electrochemical performance of the intermetallic anode is mainly due to the buffering of the stresses by this matrix. Then again, the choice of the inactive component should be carefully considered to minimise the additional weight penalty.

6.3 Tuning the solid-electrolyte interphase layer

It is the stable SEI layer that is formed on the graphite anode in lithium-ion batteries that prevents the exfoliation of graphite and has made it a commercial success. The SEI layer plays an important role in determining the cycling life of alloying anodes. A crucial role in tuning the SEI layer is played by the choice of the electrolyte. Most of the studies on sodium-ion batteries report the use of $NaClO_4$/$NaPF_6$ salts in propylene carbonate, ethylene carbonate-based solvents as the electrolyte. Recent studies have shown the advantages of using electrolyte additives such as fluoroethylene carbonate and vinylene carbonate to improve the cycling stability of alloying anodes. These additives are found to improve the quality of the SEI layer formed and thereby facilitate enhanced electrochemical performance. However, more studies on full-cell configurations as well as the optimisation of the electrolyte additives in terms of performance and cost are necessary to enable the practical applications.

6.4 Optimal choice of binder

Another strategy adopted to curb the ill-effects of huge volume expansion is the optimal choice of the binder during the electrode fabrication process. Carboxymethyl cellulose and cross-linked chitosan-based binders have been reported to provide good mechanical stability during the electrochemical (de)sodiation processes and hence improve the cycling stability when compared to polyvinylidene fluoride (PVDF). Additionally, these cellulose-based binders are water-soluble and can thus replace the use toxic solvents such as *n*-methyl-pyrrolidone used for PVDF. At times, it is necessary to apply a multi-pronged approach of the above discussed strategies to achieve good electrochemical performance for the alloying anodes. The optimal choice of these strategies can facilitate the implementation of alloying anodes for practical applications.

Summary and Outlook

To summarize, the development of high capacity anodes is quintessential to achieve the commercialization of sodium-ion batteries (SIBs) and thereby aid the cost-effective deployment of renewable energy resources. In this regard, research on alloy anodes offering the highest sodiation capacities is inevitable. Tin, antimony and phosphorous can alloy with sodium to form $Na_{15}Sn_4$, Na_3Sb and Na_3P phases respectively. These alloying reactions can occur at room temperature and hence piqued the interest of the energy storage community. Furthermore, these reactions are reversible and can aid in the deployment of batteries with high energy densities. We have discussed the recent progress in the field of alloying anodes with special emphasis on the sodiation mechanism of these potential candidates that possibly will be commercialized as this knowledge is crucial to deploy various strategies to tackle the challenges faced by alloying anodes.

These interesting Na alloying materials pose certain problems including the high volume-expansion during the formation of the sodiated phases leading to pulverization of particles and the consequent capacity fade. Hence it is quintessential to understand the sodiation mechanism of these remarkable alloying anodes and devise strategies to mitigate the challenges. We have highlighted the various approaches adopted to overcome the fundamental issue of cycling instability of alloying anodes such as the structural and morphological design of active material, use of active/inactive matrices including intermetallics and carbon-based materials to buffer volume changes during cycling and optimizing the electrolyte and binders.

We would also like to stress the fact that the studies of alloy anodes in full-cell configuration is limited and is highly necessary to facilitate the progress of commercialization of SIBs. Furthermore, the issue of low initial coulombic efficiency of alloy anodes needs to be addressed and strategies to mitigate

the same should be implemented to develop SIBs for practical applications. One of the strategies could possibly be the pre-sodiation/pre-treatment of electrodes which would reduce the penalty on the cathode. While most studies on SIBs are carried out in coin cells, the deployment of SIBs in large format cells calls for additional investigations in pouch/prismatic/cylindrical cells to analyse the issues with scale-up from the laboratory to industry. In addition, the thermal and safety aspects of SIBs have not received significant attention and need to be probed to ensure the operational safety of SIBs.

Abbreviations

NMR - Nuclear Magnetic Resonance
TEM - Transmission Electron Microscopy
XRD – X-ray diffraction
XAS- X-ray Absorption Spectroscopy
SAED – Selected Area Electron Diffraction
AFM- Atomic Force Microscopy
NVP- Sodium Vanadium Phosphate ($Na_3V_2(PO_4)_3$
CMC- Carboxymethyl Cellulose
PVDF- Polyvinylidene Fluoride
EC/DEC – Ethylene Carbonate/Diethylene Carbonate
FEC- Fluoroethylene Carbonate

Conflicts of interest

There are no conflicts to declare.

Acknowledgements

This work was financially supported by National Research Foundation of Singapore (NRF) Investigatorship award number. NRFI2017-08/ NRF2016NRF-NRFI001-22. S. S. and C. T. L. acknowledge support from the National Research Foundation, Prime Minister's Office, Singapore under medium-sized centre program and NUS-BIGHEART.

Notes and references

1 G. M. Insights, Lithium Ion Battery Market to hit $53bn by 2024: Global Market Insights Inc., https://globenewswire.com/news-release/2017/02/08/915005/0/en/Lithium-Ion-Battery-Market-to-hit-53bn-by-2024-Global-Market-Insights-Inc.html, (accessed 01-05-2018, 2018).
2 F. Risacher and B. Fritz, Aquatic Geochemistry, 2009, **15**, 123-157.
3 A. Yaksic and J. E. Tilton, Resources Policy, 2009, **34**, 185-194.
4 S. Fletcher, *Bottled lightning: superbatteries, electric cars, and the new lithium economy*, Hill and Wang, 2011.
5 M. D. Slater, D. Kim, E. Lee and C. S. Johnson, *Adv. Funct. Mater.* 2013, **23**, 947-958.
6 D. Kundu, E. Talaie, V. Duffort and L. F. Nazar, *Angew. Chem., Int. Ed.*, 2015, **54**, 3431-3448.
7 D. Larcher and J. M. Tarascon, *Nat. Chem.*, 2015, **7**, 19-29.
8 N. Yabuuchi, K. Kubota, M. Dahbi and S. Komaba, *Chem. Rev.*, 2014, **114**, 11636-11682.
9 K. Kubota and S. Komaba, *J. Electrochem. Soc.*, 2015, **162**, A2538-A2550.
10 M. Blangero, D. Carlier, M. Pollet, J. Darriet, C. Delmas and J.-P. Doumerc, *Phys. Rev. B*, 2008, **77**, 184116.
11 D. Buchholz, L. G. Chagas, M. Winter and S. Passerini, *Electrochim. Acta*, 2013, **110**, 208-213.
12 A. Caballero, L. Hernan, J. Morales, L. Sanchez, J. Santos Pena and M. A. G. Aranda, *J. Mater. Chem.*, 2002, **12**, 1142-1147.
13 M. Guignard, C. Didier, J. Darriet, P. Bordet, E. Elkaïm and C. Delmas, *Nat. Mater.*, 2013, **12**, 74-80.
14 S. Komaba, T. Nakayama, A. Ogata, T. Shimizu, C. Takei, S. Takada, A. Hokura and I. Nakai, *ECS Trans.*, 2009, **16**, 43-55.
15 S. Komaba, C. Takei, T. Nakayama, A. Ogata and N. Yabuuchi, *Electrochem. Commun.*, 2010, **12**, 355-358.
16 X. Ma, H. Chen and G. Ceder, *J. Electrochem. Soc.*, 2011, **158**, A1307-A1312.
17 D. Yuan, X. Hu, J. Qian, F. Pei, F. Wu, R. Mao, X. Ai, H. Yang and Y. Cao, *Electrochim. Acta*, 2014, **116**, 300-305.
18 J. Zhao, L. Zhao, N. Dimov, S. Okada and T. Nishida, *J. Electrochem. Soc.*, 2013, **160**, A3077-A3081.
19 J. Park, J.-S. Kim, J.-W. Park, T.-H. Nam, K.-W. Kim, J.-H. Ahn, G. Wang and H.-J. Ahn, *Electrochim. Acta*, 2013, **92**, 427-432.
20 J.-S. Kim, D.-Y. Kim, G.-B. Cho, T.-H. Nam, K.-W. Kim, H.-S. Ryu, J.-H. Ahn and H.-J. Ahn, *J. Power Sources*, 2009, **189**, 864-868.
21 J.-S. Kim, H.-J. Ahn, H.-S. Ryu, D.-J. Kim, G.-B. Cho, K.-W. Kim, T.-H. Nam and J. H. Ahn, *J. Power Sources*, 2008, **178**, 852-856.
22 K. M. Abraham, *Solid State Ionics*, 1982, **7**, 199-212.
23 M. S. Whittingham, *Prog. Solid State Chem.*, 1978, **12**, 41-99.
24 D. Dwibedi, C. D. Ling, R. B. Araujo, S. Chakraborty, S. Duraisamy, N. Munichandraiah, R. Ahuja and P. Barpanda, *ACS Appl. Mater. Interfaces*, 2016, **8**, 6982-6991.
25 P. Barpanda, *Chem. Mater.*, 2016, **28**, 1006-1011.
26 P. Barpanda, G. Oyama, S. Nishimura, S. C. Chung and A. Yamada, *Nat. Commun.*, 2014, **5**, 8.
27 I. D. Gocheva, M. Nishijima, T. Doi, S. Okada, J.-i. Yamaki and T. Nishida, *J. Power Sources*, 2009, **187**, 247-252.
28 Y. Yamada, T. Doi, I. Tanaka, S. Okada and J.-i. Yamaki, *J. Power Sources*, 2011, **196**, 4837-4841.
29 A. Kitajou, H. Komatsu, K. Chihara, I. D. Gocheva, S. Okada and J.-i. Yamaki, *J. Power Sources*, 2012, **198**, 389-392.
30 N. Dimov, A. Nishimura, K. Chihara, A. Kitajou, I. D. Gocheva and S. Okada, *Electrochim. Acta*, 2013, **110**, 214-220.
31 F. Erragh, A. Boukhari, B. Elouadi and E. M. Holt, *J. Crystallogr. Spectrosc. Res.*, 1991, **21**, 321-326.
32 P. Moreau, D. Guyomard, J. Gaubicher and F. Boucher, *Chem. Mater.*, 2010, **22**, 4126-4128.
33 K. T. Lee, T. N. Ramesh, F. Nan, G. Botton and L. F. Nazar, *Chem. Mater.*, 2011, **23**, 3593-3600.
34 K. Zaghib, J. Trottier, P. Hovington, F. Brochu, A. Guerfi, A. Mauger and C. M. Julien, *J. Power Sources*, 2011, **196**, 9612-9617.
35 P. Barpanda, T. Ye, S.-i. Nishimura, S.-C. Chung, Y. Yamada, M. Okubo, H. Zhou and A. Yamada, *Electrochem. Commun.*, 2012, **24**, 116-119.
36 T. Honma, T. Togashi, N. Ito and T. Komatsu, *J. Ceram. Soc. Jpn*, 2012, **120**, 344-346.
37 A. Sun, F. R. Beck, D. Haynes, J. A. Poston, S. R. Narayanan, P. N. Kumta and A. Manivannan, *Mater. Sci. Eng., B*, 2012, **177**, 1729-1733.
38 R. K. B. Gover, A. Bryan, P. Burns and J. Barker, *Solid State Ionics*, 2006, **177**, 1495-1500.
39 Y. Kawabe, N. Yabuuchi, M. Kajiyama, N. Fukuhara, T. Inamasu, R. Okuyama, I. Nakai and S. Komaba, *Electrochem. Commun.*, 2011, **13**, 1225-1228.
40 Y.-U. Park, D.-H. Seo, H.-S. Kwon, B. Kim, J. Kim, H. Kim, I. Kim, H.-I. Yoo and K. Kang, *J. Am. Chem. Soc.*, 2013, **135**, 13870-13878.

41 Y. Lu, S. Zhang, Y. Li, L. Xue, G. Xu and X. Zhang, *J. Power Sources*, 2014, **247**, 770-777.
42 M. M. Doeff, Y. Ma, S. J. Visco and L. C. De Jonghe, *J. Electrochem. Soc.*, 1993, **140**, L169-L170.
43 D. A. Stevens and J. R. Dahn, *J. Electrochem. Soc.*, 2000, **147**, 1271-1273.
44 Y. Kim, K. H. Ha, S. M. Oh and K. T. Lee, *Chem. – Eur. J.*, 2014, **20**, 11980-11992.
45 M. Mortazavi, Q. Ye, N. Birbilis and N. V. Medhekar, *J. Power Sources*, 2015, **285**, 29-36.
46 M.-S. Balogun, Y. Luo, W. Qiu, P. Liu and Y. Tong, *Carbon*, 2016, **98**, 162-178.
47 H. Hou, C. E. Banks, M. Jing, Y. Zhang and X. Ji, *Adv. Mater.*, 2015, **27**, 7861-7866.
48 Y. Zhang, C. W. Foster, C. E. Banks, L. Shao, H. Hou, G. Zou, J. Chen, Z. Huang and X. Ji, Adv. Mater., 2016, **28**, 9391-9399.
49 H. Hou, L. Shao, Y. Zhang, G. Zou, J. Chen and X. Ji, Advanced Sci., 2016, **4**, 1600243.
50 M. Sawicki and L. L. Shaw, *RSC Adv.*, 2015, **5**, 53129-53154.
51 M. H. Han, E. Gonzalo, G. Singh and T. Rojo, *Energy Environ. Sci.*, 2015, **8**, 81-102.
52 S.-W. Kim, D.-H. Seo, X. Ma, G. Ceder and K. Kang, *Adv. Energy Mater.*, 2012, **2**, 710-721.
53 V. Palomares, P. Serras, I. Villaluenga, K. B. Hueso, J. Carretero-González and T. Rojo, *Energy Environ. Sci.*, 2012, **5**, 5884.
54 W. Luo, F. Shen, C. Bommier, H. Zhu, X. Ji and L. Hu, *Acc. Chem. Res.*, 2016, **49**, 231-240.
55 C. Bommier and X. Ji, *Isr. J.Chem.*, 2015, **55**, 486-507.
56 H. Pan, Y.-S. Hu and L. Chen, *Energy Environ. Sci.*, 2013, **6**, 2338.
57 B. L. Ellis and L. F. Nazar, *Curr. Opin. Solid State Mater. Sci.*, 2012, **16**, 168-177.
58 V. Palomares, M. Casas-Cabanas, E. Castillo-Martínez, M. H. Han and T. Rojo, *Energy Environ. Sci.*, 2013, **6**, 2312.
59 V. L. Chevrier and G. Ceder, *J. Electrochem. Soc.*, 2011, **158**, A1011.
60 S. Komaba, Y. Matsuura, T. Ishikawa, N. Yabuuchi, W. Murata and S. Kuze, *Electrochem. Commun.*, 2012, **21**, 65-68.
61 L. D. Ellis, T. D. Hatchard and M. N. Obrovac, *J. Electrochem. Soc.*, 2012, **159**, A1801-A1805.
62 J. M. Stratford, M. Mayo, P. K. Allan, O. Pecher, O. J. Borkiewicz, K. M. Wiaderek, K. W. Chapman, C. J. Pickard, A. J. Morris and C. P. Grey, *J. Am. Chem. Soc.*, 2017, **139**, 7273-7286.
63 J. W. Wang, X. H. Liu, S. X. Mao and J. Y. Huang, *Nano Lett.*, 2012, **12**, 5897-5902.
64 B. A. Zhang, G. Rousse, D. Foix, R. Dugas, D. A. D. Corte and J. M. Tarascon, *Adv. Mater.*, 2016, **28**, 9824-9830.
65 C. Kim, K. Y. Lee, I. Kim, J. Park, G. Cho, K. W. Kim, J. H. Ahn and H. J. Ahn, *J. Power Sources*, 2016, 317, 153-158.
66 B. Luo, T. F. Qiu, D. L. Ye, L. Z. Wang and L. J. Zhi, *Nano Energy*, 2016, **22**, 232-240.
67 M. Sha, H. Zhang, Y. T. Nie, K. Q. Nie, X. X. Lv, N. Sun, X. K. Xie, Y. Y. Ma and X. H. Sun, *J. Mater. Chem. A*, 2017, **5**, 6277-6283.
68 Y. Jeon, X. G. Han, K. Fu, J. Q. Dai, J. H. Kim, L. B. Hu, T. Song and U. Paik, *J. Mater. Chem. A*, 2016, **4**, 18306-18313.
69 S. T. Li, Z. M. Wang, J. Liu, L. Y. Yang, Y. Guo, L. Z. Cheng, M. Lei and W. J. Wang, *ACS Appl. Mater. Interfaces*, 2016, **8**, 19438-19445.
70 T.-H. Kim, K.-S. Hong, D. Sohn, M. Kim, D.-H. Nam, E. Cho and H. Kwon, *J. Mater. Chem. A*, 2017, **5**, 20304-20315.
71 D. N. Lan, W. H. Wang, L. Shi, Y. Huang, L. B. Hu and Q. Li, *J. Mater. Chem. A*, 2017, **5**, 5791-5796.
72 Q. Li, Z. Q. Li, Z. W. Zhang, C. X. Li, J. Y. Ma, C. X. Wang, X. L. Ge, S. H. Dong and L. W. Yin, *Adv. Energy Mater.*, 2016, **6**, 10.
73 Y. Xu, B. Peng and M. Mulder Fokko, *Adv. Energy Mater.*, 2017, **8**, 1701847.
74 A.-R. Park and C.-M. Park, ACS Nano, 2017, 11, 6074-6084.
75 L. O. Vogt and C. Villevieille, *J. Mater. Chem. A*, 2016, **4**, 19116-19122.
76 E. Edison, W. C. Ling, V. Aravindan and S. Madhavi, *ChemElectroChem*, 2017, **4**, 1932-1936.
77 X. Yang, R. Zhang, N. Chen, X. Meng, P. Yang, C. Wang, Y. Zhang, Y. Wei, G. Chen and F. Du, *Chem. – Eur. J.*, 2016, **22**, 1445-1451.
78 F. Zhang, C. Xia, J. Zhu, B. Ahmed, H. Liang, D. B. Velusamy, U. Schwingenschlögl and H. N. Alshareef, *Adv. Energy Mater.*, 2016, **6**, 1601188
79 B. Huang, J. Yang, Y. Li, S. Xiao and Q. Chen, *Mater. Lett.*, 2018, **210**, 321-324.
80 L. Baggetto, H. Y. Hah, J. C. Jumas, C. E. Johnson, J. A. Johnson, J. K. Keum, C. A. Bridges and G. M. Veith, *J. Power Sources*, 2014, **267**, 329-336.
81 A. Darwiche, C. Marino, M. T. Sougrati, B. Fraisse, L. Stievano and L. Monconduit, *J. Am. Chem. Soc.*, 2013, **135**, 10179-10179.
82 P. K. Allan, J. M. Griffin, A. Darwiche, O. J. Borkiewicz, K. M. Wiaderek, K. W. Chapman, A. J. Morris, P. J. Chupas, L. Monconduit and C. P. Grey, *J. Am. Chem. Soc.*, 2016, **138**, 2352-2365.
83 L. Baggetto, P. Ganesh, C.-N. Sun, R. A. Meisner, T. A. Zawodzinski and G. M. Veith, *J. Mater. Chem. A*, 2013, **1**, 7985-7994.
84 L. Wu, X. Hu, J. Qian, F. Pei, F. Wu, R. Mao, X. Ai, H. Yang and Y. Cao, *Energy Environ. Sci.*, 2014, **7**, 323-328.
85 J. Liu, L. Yu, C. Wu, Y. Wen, K. Yin, F.-K. Chiang, R. Hu, J. Liu, L. Sun, L. Gu, J. Maier, Y. Yu and M. Zhu, Nano Lett., 2017, 17, 2034-2042.
86 J. Gu, Z. Du, C. Zhang, J. Ma, B. Li and S. Yang, Adv. Energy Mater., 2017, 7, 1700447.
87 H. C. Gao, W. D. Zhou, J. H. Jang and J. B. Goodenough, *Adv. Energy Mater.*, 2016, **6**, 7.
88 H. S. Hou, M. J. Jing, Y. Zhang, J. Chen, Z. D. Huang and X. B. Ji, *J. Mater. Chem. A*, 2015, **3**, 17549-17552.
89 H. S. Hou, M. J. Jing, Y. C. Yang, Y. Zhang, W. X. Song, X. M. Yang, J. Chen, Q. Y. Chen and X. B. Ji, *J. Power Sources*, 2015, **284**, 227-235.
90 C. W. Lee, J. C. Kim, S. Park, H. J. Song and D. W. Kim, *Nano Energy*, 2015, **15**, 479-489.
91 N. Zhang, Y. C. Liu, Y. Y. Lu, X. P. Han, F. Y. Cheng and J. Chen, *Nano Res.*, 2015, **8**, 3384-3393.
92 F. Wan, J. Z. Guo, X. H. Zhang, J. P. Zhang, H. Z. Sun, Q. Y. Yan, D. X. Han, L. Niu and X. L. Wu, *ACS Appl. Mater. Interfaces*, 2016, **8**, 7790-7799.
93 Y. J. Zhu, X. G. Han, Y. H. Xu, Y. H. Liu, S. Y. Zheng, K. Xu, L. B. Hu and C. S. Wang, *ACS Nano*, 2013, **7**, 6378-6386.
94 C. Wu, L. Shen, S. Chen, Y. Jiang, P. Kopold, P. A. van Aken, J. Maier and Y. Yu, *Energy Storage Materials*, 2018, **10**, 122-129.
95 M. He, M. Walter, K. V. Kravchyk, R. Erni, R. Widmer and M. V. Kovalenko, *Nanoscale*, 2015, **7**, 455-459.
96 L. Ji, W. Zhou, V. Chabot, A. Yu and X. Xiao, *ACS Appl. Mater. Interfaces*, 2015, **7**, 24895-24901.
97 H. Gao, J. Niu, C. Zhang, Z. Peng and Z. Zhang, *ACS Nano*, 2018, **12**, 3568-3577.
98 L. B. Wang, C. C. Wang, N. Zhang, F. J. Li, F. Y. Cheng and J. Chen, *ACS Energy Lett.*, 2017, **2**, 256-262.
99 J. Liu, Z. Z. Yang, J. Q. Wang, L. Gu, J. Maier and Y. Yu, *Nano Energy*, 2015, **16**, 389-398.
100 E. Edison, S. Sreejith and S. Madhavi, *ACS Appl. Mater. Interfaces*, 2017, **9**, 39399-39406.
101 A. M. Nie, L. Y. Gan, Y. C. Cheng, X. Y. Tao, Y. F. Yuan, S. Sharifi-Asl, K. He, H. Asayesh-Ardakani, V. Vasiraju, J. Lu, F. Mashayek, R. Klie, S. Vaddiraju, U. Schwingenschlogl and R. Shahbazian-Yassar, *Adv. Funct. Mater.*, 2016, **26**, 543-552.

102 E. D. Jackson, S. Green and A. L. Prieto, *ACS Appl. Mater. Interfaces*, 2015, **7**, 7447-7450.
103 K. P. S. S. Hembram, H. Jung, B. C. Yeo, S. J. Pai, S. Kim, K.-R. Lee and S. S. Han, *J. Phys. Chem. C*, 2015, **119**, 15041-15046.
104 M. Mayo, K. J. Griffith, C. J. Pickard and A. J. Morris, *Chem. Mater.*, 2016, **28**, 2011-2021.
105 C. Zhang, X. Wang, Q. Liang, X. Liu, Q. Weng, J. Liu, Y. Yang, Z. Dai, K. Ding, Y. Bando, J. Tang and D. Golberg, *Nano Lett.*, 2016, **16**, 2054-2060.
106 M. Dahbi, N. Yabuuchi, M. Fukunishi, K. Kubota, K. Chihara, K. Tokiwa, X.-f. Yu, H. Ushiyama, K. Yamashita, J.-Y. Son, Y.-T. Cui, H. Oji and S. Komaba, *Chem. Mater.*, 2016, **28**, 1625-1635.
107 J. Zhou, X. Liu, W. Cai, Y. Zhu, J. Liang, K. Zhang, Y. Lan, Z. Jiang, G. Wang and Y. Qian, *Adv. Mater.*, 2017, **29**, 1700214.
108 H. Gao, T. Zhou, Y. Zheng, Y. Liu, J. Chen, H. Liu and Z. Guo, *Adv. Energy Mater.*, 2016, **6**, 1601037.
109 J. Qian, X. Wu, Y. Cao, X. Ai and H. Yang, *Angew. Chem., Int. Ed.*, 2013, **52**, 4633-4636.
110 Y. Kim, Y. Park, A. Choi, N.-S. Choi, J. Kim, J. Lee, J. H. Ryu, S. M. Oh and K. T. Lee, *Adv. Mater.*, 2013, **25**, 3045-3049.
111 J. Sun, H.-W. Lee, M. Pasta, H. Yuan, G. Zheng, Y. Sun, Y. Li and Y. Cui, *Nat. Nanotechnol.*, 2015, **10**, 980-985.
112 Y. Liu, A. Zhang, C. Shen, Q. Liu, X. Cao, Y. Ma, L. Chen, C. Lau, T.-C. Chen, F. Wei and C. Zhou, *ACS Nano*, 2017, 11, 5530-5537.
113 S.-O. Kim and A. Manthiram, *Chem. Mater.*, 2016, **28**, 5935-5942.
114 W.-J. Li, S.-L. Chou, J.-Z. Wang, H.-K. Liu and S.-X. Dou, *Chem. Commun.*, 2015, **51**, 3682-3685.
115 J. Fullenwarth, A. Darwiche, A. Soares, B. Donnadieu and L. Monconduit, *J. Mater. Chem. A*, 2014, **2**, 2050-2059.
116 W.-J. Li, Q.-R. Yang, S.-L. Chou, J.-Z. Wang and H.-K. Liu, *J. Power Sources*, 2015, **294**, 627-632.
117 D. Duveau, S. S. Israel, J. Fullenwarth, F. Cunin and L. Monconduit, *J. Mater. Chem. A*, 2016, **4**, 3228-3232.
118 H. Okamoto, L. Kacprzak and P. Subramanian, Binary Alloy Phase Diagrams*, ASM International*, 1996.
119 L. D. Ellis, B. N. Wilkes, T. D. Hatchard and M. N. Obrovac, *J. Electrochem. Soc.*, 2014, **161**, A416-A421.
120 D. Su, S. Dou and G. Wang, *Nano Energy*, 2015, **12**, 88-95.
121 J. Sottmann, M. Herrmann, P. Vajeeston, Y. Hu, A. Ruud, C. Drathen, H. Emerich, H. Fjellvåg and D. S. Wragg, *Chem. Mater.*, 2016, **28**, 2750-2756.
122 J. Songster and A. D. Pelton, *J. Phase Equilib.*, 1992, **13**, 67-69.
123 Q. Zhao, Y. Huang and X. Hu, *Electrochem. Commun.*, 2016, **70**, 8-12.
124 C.-H. Lim, T.-Y. Huang, P.-S. Shao, J.-H. Chien, Y.-T. Weng, H.-F. Huang, B. J. Hwang and N.-L. Wu, *Electrochim. Acta*, 2016, **211**, 265-272.
125 L. Zhang, X. Hu, C. Chen, H. Guo, X. Liu, G. Xu, H. Zhong, S. Cheng, P. Wu, J. Meng, Y. Huang, S. Dou and H. Liu, *Adv. Mater.*, 2017, **29**, 1604708.
126 X. Xiao, X. Li, S. Zheng, J. Shao, H. Xue and H. Pang, *Adv. Mater. Interfaces*, 2017, **4**, 1600798.
127 L. Baggetto, J. K. Keum, J. F. Browning and G. M. Veith, *Electrochem. Commun.*, 2013, **34**, 41-44.
128 B. Farbod, K. Cui, W. P. Kalisvaart, M. Kupsta, B. Zahiri, A. Kohandehghan, E. M. Lotfabad, Z. Li, E. J. Luber and D. Mitlin, *ACS Nano*, 2014, **8**, 4415-4429.
129 P. R. Abel, Y.-M. Lin, T. de Souza, C.-Y. Chou, A. Gupta, J. B. Goodenough, G. S. Hwang, A. Heller and C. B. Mullins, *J. Phys. Chem. C*, 2013, **117**, 18885-18890.
130 A. Kohandehghan, K. Cui, M. Kupsta, J. Ding, E. Memarzadeh Lotfabad, W. P. Kalisvaart and D. Mitlin, *Nano Lett.*, 2014, **14**, 5873-5882.
131 X. Lu, E. R. Adkins, Y. He, L. Zhong, L. Luo, S. X. Mao, C.-M. Wang and B. A. Korgel, *Chem. Mater.*, 2016, **28**, 1236-1242.
132 Q. Li, Z. Zhang, S. Dong, C. Li, X. Ge, Z. Li, J. Ma and L. Yin, *Part. Part. Syst. Charact.*, 2017, **34**, 1600115.

TOC Graphics: